ACS Catalysis

Research Article

pubs.acs.org/acscatalysis

Computational Design of Alloy-Core@Shell Metal Nanoparticle Catalysts

Liang Zhang and Graeme Henkelman*

Department of Chemistry and the Institute for Computational Engineering and Sciences, The University of Texas at Austin, 1 University Station A5300, Austin, Texas 78712-0165, United States

Supporting Information

ABSTRACT: The alloy-core@shell nanoparticle structure combines the advantages of a robust noble-metal shell and a tunable alloy-core composition. In this study we demonstrate a set of linear correlations between the binding of adsorbates to the shell and the alloy-core composition, which are general across a range of nanoparticle compositions, size, and adsorbate molecules. This systematic tunability allows for a simple approach to the design of such catalysts. Calculations of candidate structures for the hydrogen evolution reaction predict a high activity for the PtRu@Pd structure, in good agreement with what has been reported previously. Calculations of alloy-core@Pt 140-atom nanoparticles reveal new candidate structures for CO oxidation at high temperature, including $Au_{0.65}Pd_{0.35}$@Pt and $Au_{0.73}Pt_{0.27}$@Pt, which are predicted to have reaction rates 200 times higher than that of Pt(111).

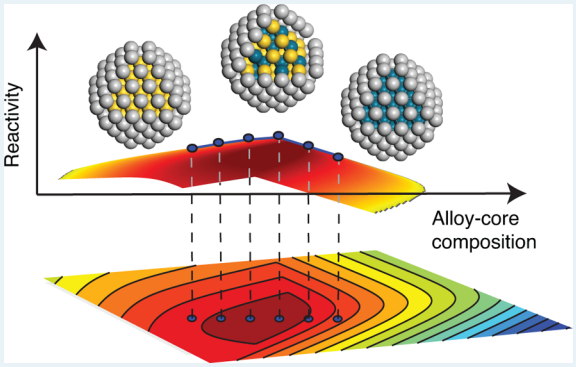

KEYWORDS: *alloy-core/shell, nanoparticles, binding energy, catalyst design, hydrogen evolution, CO oxidation*

1. INTRODUCTION

A promising geometry for new nanoparticle catalysis has a homogeneous noble-metal shell around a random alloy core of tunable composition.[1,2] The noble shell protects the particle core during the catalytic processes, and the alloy-core composition allows for fine tuning of the catalytic properties.[3,4] Alloy-core@shell nanoparticles can be synthesized by covering a random-alloy nanoparticle with the thin layer of the shell metal. There are two common synthetic techniques for this. The first is acid leaching of the non-noble-metal component in the shell and thermal treatment to form a noble-metal skin. Examples of this include Pt_3M for M = Fe, Ni, Co. These bimetallic alloys covered with a Pt-skin, that were synthesized by Stamenkovic and co-workers, exhibited an improved oxygen reduction reaction (ORR) activity versus conventional Pt catalysts.[5−8] Second, under potential deposition (UPD) can be used to form a homogeneous monolayer shell on the core via careful potential control.[9−12] Recent work in Adzic's group,[13,14] and ours,[1] demonstrated successful synthesis of PdAu@Pt nanoparticles by Cu UPD on a PdAu core with subsequent galvanic exchange of the Cu with Pt.

Previous work shows that there is a nearly linear correlation between the O binding energy on alloy-core@shell nanoparticles and the alloy-core composition.[1,2] In this paper, we demonstrate that this linear correlation extends to many different adsorbates, and holds for geometries ranging from small nanoparticles to single crystal surfaces. Thus, the adsorbate binding on alloy-core@shell nanoparticle X_xY_{1-x}@Z can be estimated from the two corresponding single-core@shell nanoparticles X@Z and Y@Z end point structures via interpolation

$$Eb_{X_xY_{1-x}@Z} \approx xEb_{X@Z} + (1 - x)Eb_{Y@Z} \quad (1)$$

where $Eb_{X@Z}$ and $Eb_{Y@Z}$ are the binding energies of the adsorbate on the core@shell nanoparticles X@Z and Y@Z and x is the ratio of component X in the XY random alloy core of the X_xY_{1-x}@Z particle. Many studies over the past decade have shown that the activity of catalytic reactions can be well described by the binding energies of key adsorbates on the catalyst.[15−18] Given the correlation between binding energy and activity, we are able to optimize the compositions of alloy-core@shell nanoparticles for certain catalytic reactions. Specifically, the hydrogen evolution reaction (HER) and CO oxidation (COox) are considered in this work to demonstrate how the alloy-core@shell structures can be tuned for catalysis.

2. COMPUTATIONAL MODELS AND METHODS

In this study, adsorbate binding energies were calculated with density functional theory (DFT), as implemented in the Vienna ab initio simulation package.[19,20] Core electrons were described using the projector augmented wave method.[21,22] Kohn−Sham single-electron wave functions were expanded in a plane wave basis with a kinetic energy cutoff of 300 eV to describe the valence electrons. The generalized gradient approximation

Received: August 11, 2014
Revised: December 9, 2014
Published: December 12, 2014

DOI: 10.1021/cs501176b
ACS Catal. 2015, 5, 655−660

using the revised Perdew–Burke–Ernzerhof functional[23] was chosen to evaluate the exchange-correlation energy. Spin polarization was tested and was used when necessary. All atoms in the nanoparticle were allowed to relax; geometries were considered optimized when the force on each atom was less than 0.01 eV/Å.

Linear correlations between alloy-core compositions and the binding energy of adsorbates A (A = O, C, H, N, S, CO, NO) were examined. Two geometries were studied, a nanoparticle containing 140 atoms and a face-centered-cubic (FCC) single-crystal (111) surface with a Pt monolayer skin covering a Pd/Au random alloy, as illustrated in Figure 1. The nanoparticles

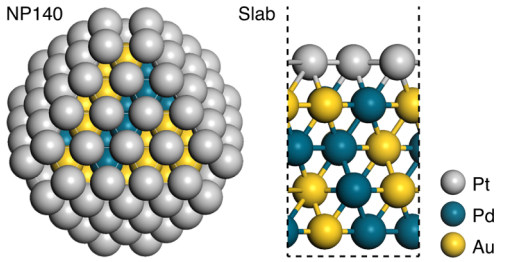

Figure 1. Structures of the PdAu@Pt NP140 and slab models.

were modeled as FCC crystallites in the shape of a truncated octahedron (denoted as NP140) with 44 core and 96 shell atoms. A cubic box of side length 26 Å was used to contain the particle with a vacuum gap of 11 Å in all directions to avoid interactions from periodic images. A Γ-point sampling of the Brillouin zone was used for the isolated particles. Convergence was checked by increasing the energy cutoff to 400 eV and the *k*-point mesh sampling to 2 × 2 × 2; the oxygen binding energy on a Pt 140-atom nanoparticle was found to change by only 1 meV (<0.1%). For each configuration, an adsorbate atom or molecule was bound to the center of each (111) facet, giving eight adsorbates in total. The binding energy Eb of adsorbate A was calculated by averaging over these eight sites as

$$\mathrm{Eb} = \frac{1}{8}(E_{\mathrm{NP+8A}} - E_{\mathrm{NP}} - 8E_{\mathrm{A}}) \quad (2)$$

where $E_{\mathrm{NP+8A}}$ is the energy of the particle with eight bound adsorbates A, E_{NP} is the energy of the bare particle, and E_{A} is the reference energy of the adsorbate, A.

Single-crystal surfaces were modeled with five-layer (3 × 3) slabs, to simulate the (111) facets of large nanoparticles.[24,25] The bottom four layers consisted of a PdAu random alloy, and the topmost layer contained monometallic Pt. A surface of this size and a vacuum gap of at least 12 Å between slabs was used to isolate the adsorbates from their periodic images. A (4 × 4 × 1) Monkhorst–Pack *k*-point mesh was used to sample the Brillouin zone. In all calculations, the bottom two layers of the slab were held frozen in their lattice positions. For each configuration, the binding energy of adsorbate A on the nine different FCC hollow sites are calculated as

$$\mathrm{Eb} = E_{\mathrm{slab+A}} - E_{\mathrm{slab}} - E_{\mathrm{A}} \quad (3)$$

For both the NP140 and slab models, binding of O, C, H, N, S, and NO was studied on the FCC-hollow sites of the (111) facet, while CO was bound to on-top sites. Details about the reference energies of the adsorbates, E_{A}, are given in the Supporting Information. CO adsorption energies are corrected on the basis of the CO stretching frequency as proposed by Mason.[26] Ten different random-alloy configurations were generated to calculate the average binding energy for each core composition, giving a total of 80 binding sites for the nanoparticle and 90 sites for the slab model, contributing to the average. Although the number of random configurations considered is less than the total possible number, our sampling is sufficient for capturing trends in binding energies (see Figure S1, Supporting Information).

3. RESULTS AND DISCUSSION

3.1. Linear Binding Energy Correlation. Trends in the binding energy of the seven adsorbates were calculated as a function of composition in a Pd/Au subsurface alloy, covered with a monolayer of Pt. As demonstrated by Nørskov et al., there is a good scaling relationship between a single atomic adsorbate and its hydrides with the same binding geometry, e.g. O vs OH, C vs CH_n, and N vs NH_n.[27,28] Accordingly, the seven adsorbates were chosen to cover most of the key reactant motifs of interest for heterogeneous catalysis related to energy. Figure 2 shows the average binding energy of the adsorbates on

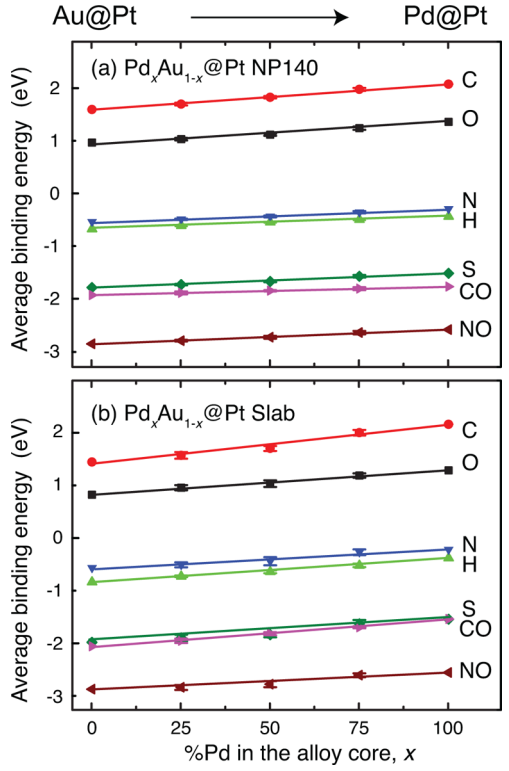

Figure 2. Average binding energy of seven adsorbates to the Pt(111) facets of Pd_xAu_{1-x}@Pt (a) NP140 and (b) slab geometries as a function of the Pd ratio in the alloy core, *x*.

the Pd_xAu_{1-x}@Pt NP140 and slab geometries with Pd ratios *x* = 0, 0.25, 0.5, 0.75 and 1.0, in the random alloy core. The standard deviation of the binding energy distribution is indicated by the error bars. The linear relationship between the binding energy and core composition is a result of the linear response of shell *d*-band center shift to the variation of the alloy-core composition. Figure 3 shows that the average *d*-band center of PdAu@Pt NP140 also varies linearly with the alloy-core composition. Increasing the ratio of Pd in the alloy core gradually lowers the *d*-band center of the Pt shell, which leads to a linearly weakened adsorbate binding, as shown in Figure 2.

DOI: 10.1021/cs501176b
ACS Catal. 2015, 5, 655–660

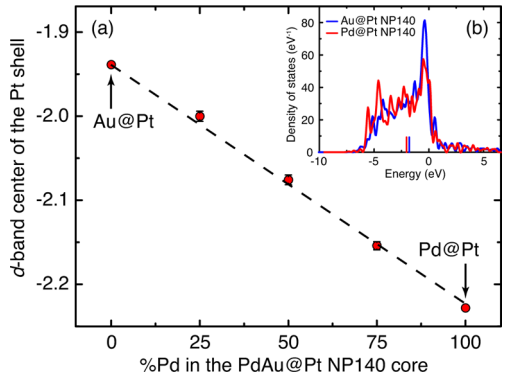

Figure 3. (a) Average *d*-band center (red circles) of the Pt shell varying linearly with the fraction of Pd in the alloy-core, *x*, in Pd_xAu_{1-x}@Pt NP140. (b) *d*-band density of states for the Pt shell at the two end point structures: Au@Pt (blue) and Pd@Pt (red) NP140. The small vertical marks above the *x* axis indicate the center of the *d*-bands. The Pd core lowers the *d*-band of the Pt shell in comparison with the Au core.

Similar linear correlation trends between the core composition and the *d*-band center of the shell was observed previously for the PdCu@Pd system.[2] In that work, it was shown that strain and charge redistribution are two major factors affecting the *d*-band of the nanoparticle shell. In the PdCu@Pd system, the two effects had a similar influence on the *d*-band center, but in general their relative weight will depend upon the specific metals. In the PdAu@Pt system, for example, the *d*-band center shift is dominated by strain effects. Charge redistribution is much more important in the PdIr@Pt system, where the variation in Pt−Pt bond lengths is much smaller. Details of these extreme examples are given in Figure S4, Supporting Information.

3.2. Alloy-Core Composition Optimization. We have shown there is a general linear correlation between the core composition and adsorbate binding of alloy-core@shell nanoparticles. In order to optimize the composition for catalytic reactions of interest, we need a model that correlates adsorbate binding with the overall catalytic activity. In the past decade, much work has been done to reduce the number of parameters used to describe the activity of complex reactions. Nørskov et al. proposed a systematic method to construct the Sabatier rate as a function of the binding energy of one or two key reactants using mean-field microkinetic models.[29−31] Building upon on the adsorption energy scaling and Brønsted−Evans−Polanyi (BEP) relationships, this "Sabatier analysis method" significantly reduces the number of parameters and computational effort required for materials screening.

In the alloy-core@shell system, the binding energies of adsorbates are all functions of the alloy-core composition. Two properties of alloy-core@shell structures give rise to advantages in catalyst design. First, the number of descriptors for the reaction can be reduced to just one, that is the alloy-core composition. Second, the core composition with a desired adsorbate binding energy can be determined from the single-core@shell structures. In other words, by calculating adsorbate binding to the single-core@shell structures, we are able to explore the parameter space of alloy cores connected by any two structures with the same shell metal.

Following the theoretical framework of Nørskov et al., the Sabatier rate of a reaction $r_s(\mathbf{v})$ is constructed as a function of the reactivity descriptors $\{Eb^i\}$, where $\mathbf{v} = \{Eb^1, Eb^2, ..., Eb^n\}$ is the descriptor vector and Eb^i is the binding energy of key adsorbate. For the alloy-core@shell structures X_xY_{1-x}@Z, the descriptor vector at an intermediate alloy-core composition *x* can be estimated from a linear interpolation between the two single-core@shell structures as

$$\mathbf{v}(x) = x\mathbf{v}_{X@Z} + (1 - x)\mathbf{v}_{Y@Z} \tag{4}$$

where $\mathbf{v}_{X@Z}$ and $\mathbf{v}_{Y@Z}$ are the descriptor vectors of X@Z and Y@Z, respectively. The Sabatier rate is then expressed as a function of alloy-core composition *x*, and the extremum of the reaction rate of X_xY_{1-x}@Z is achieved where

$$\frac{\partial r_s}{\partial x} = \frac{\partial r_s}{\partial \mathbf{v}}\frac{\partial \mathbf{v}}{\partial x} = \nabla r_s \cdot (\mathbf{v}_{X@Z} - \mathbf{v}_{Y@Z}) = 0 \tag{5}$$

In principle, the extremum composition can be obtained analytically by solving eq 5, where the gradient of the rate is normal to the vector connecting the two single-core@shell compositions. In a special case where the dimension of the descriptor vector is 1, e.g. the ORR and HER, where the catalytic activity of the reaction can be described by the binding energy Eb of a single adsorbate,[32,33] eq 5 can be simplified as $\nabla r = (dr_s)/(dEb) = 0$. If the reaction rate reaches its extremum at Eb*, where $((dr_s)/(dEb)) = 0$, then the composition *x** with the extreme rate is

$$x^* = \frac{Eb^* - Eb_{Y@Z}}{Eb_{X@Z} - Eb_{Y@Z}} \tag{6}$$

To have $x^* \in [0, 1]$, the condition $(Eb^* - Eb_{X@Z})(Eb^* - Eb_{Y@Z}) < 0$ must be satisfied. In other words, X@Z and Y@Z must be on different sides of the volcano peak.

The above optimization scheme works on the basis of linear binding energy correlations for alloy-core@shell nanoparticles, as well as models that correlate binding with the catalytic activity. There are a couple of approximations in this approach which should be highlighted. First, in binding energy calculations the random alloy-core compositions were held fixed. Thus, effects of large geometric deformations due to variations of composition are not considered in our model. Structural rearrangements and alloy-core segregation may cause deviations from the linear correlations presented. Second, the BEP relations and Sabatier analysis are essential to obtain the correlation of descriptors and activity. Uncertainties in either approximation will affect the accuracy of this optimization scheme.

Table 1. Free Energy of Adsorption for Hydrogen ΔG_H (eV) on a Variety of Pd- and Pt-Shelled Slabs

	core metal							
structure	Au	Ag	Pd	Pt	Ir	Rh	Ru	Cu
Pd-shell	−0.25	−0.22	−0.18	−0.18	0.10	0.11	0.17	0.25
Pt-shell	−0.27	−0.24	−0.11	−0.05	0.22	0.24	0.33	0.41

DOI: 10.1021/cs501176b
ACS Catal. 2015, 5, 655−660

3.3. Hydrogen Evolution Reaction. The HER is the cathode reaction in water electrolysis, where hydrogen is produced from proton reduction. It was first proposed by Parsons that the free energy of hydrogen adsorption ΔG_H is a good reaction descriptor of the HER, and the optimal activity is near $\Delta G_H = 0.0$ eV.[34] With well-defined approximations for the zero-point energy and entropy, the free energy of hydrogen adsorption on different surfaces can be calculated as $\Delta G_H = Eb_H + 0.24$ eV, where Eb_H is the binding energy of hydrogen atom on the surface.[33] Since this 0.24 eV shift is constant for different surfaces, the alloy-core composition optimization strategy of eq 6 is applicable to the HER. Table 1 gives the free energy of adsorption for hydrogen on a variety of single-core@Pd-shelled and Pt-shelled slabs. For both Pd- and Pt-shelled slabs, the free energy of adsorption is negative when the core is Au, Ag, Pd, or Pt, and it is positive with cores of Ir, Rh, Ru, and Cu. In order to satisfy $x^* \in [0, 1]$, a metal X must be selected from {Au, Ag, Pd, Pt} and a metal Y from {Ir, Rh, Ru, Cu} to form an optimal alloy core. ΔG_H on X_xY_{1-x}@Z (X = Au, Ag, Pd, Pt; Y = Ir, Rh, Ru, Cu; Z = Pd, Pt) will be tuned to 0, when the ratio of X in the alloy core is x^*. Table 2 gives the optimal compositions x^*. Notably, Table 2 shows that PtRu@Pd has the best HER performance at a Pt:Ru ratio of 1:1 in the alloy core. This is in a good agreement with previous reports by Greeley et al.[35,36]

Table 2. Optimal Ratio x^* of Metal X Alloyed with Metal Y in the Core of Pd- and Pt-Covered Slabs for the HER

	metal X							
	Pd-shell				Pt-shell			
metal Y	Au	Ag	Pd	Pt	Au	Ag	Pd	Pt
Ir	0.71	0.69	0.64	0.64	0.55	0.52	0.33	0.19
Rh	0.69	0.67	0.62	0.62	0.53	0.50	0.31	0.17
Ru	0.60	0.56	0.51	0.51	0.45	0.42	0.25	0.13
Cu	0.50	0.47	0.42	0.42	0.40	0.37	0.21	0.11

3.4. CO Oxidation. CO oxidation has been widely studied as a model catalytic reaction on a wide variety of systems, such as metal surfaces, clusters, and supported metal clusters. There are two primary reaction mechanisms involved: (1) the dissociative mechanism (R1−R4), consisting of O_2 dissociation and subsequent association with CO to form CO_2, and (2) the associative mechanism (R5), which is active when the pressure of O_2 is high enough and the O_2 molecules can oxidize CO directly without dissociation.[15,37]

$$CO + * \Leftrightarrow CO* \quad (R1)$$

$$O_2 + * \Leftrightarrow O_2* \quad (R2)$$

$$O_2^* + * \Leftrightarrow 2O* \quad (R3)$$

$$CO* + O* \Leftrightarrow CO_2 + 2* \quad (R4)$$

$$CO* + O_2* \Leftrightarrow CO_2 + O* + * \quad (R5)$$

On the basis of these mechanisms (R1−R5), Falsig et al. built a volcano plot of the Sabatier rate over a closed-packed metal surface as a function of the O and CO binding energies, Eb[O] and Eb[CO].[15] In this work, we have calculated Eb[O] and Eb[CO] for several single-core@Pt-shell NP140 and explored potential alloy-core@shell structures for CO oxidation on the basis of Falsig's Sabatier rate model. In Figure 4 we reproduce Falsig's contour plot of relative Sabatier activity for

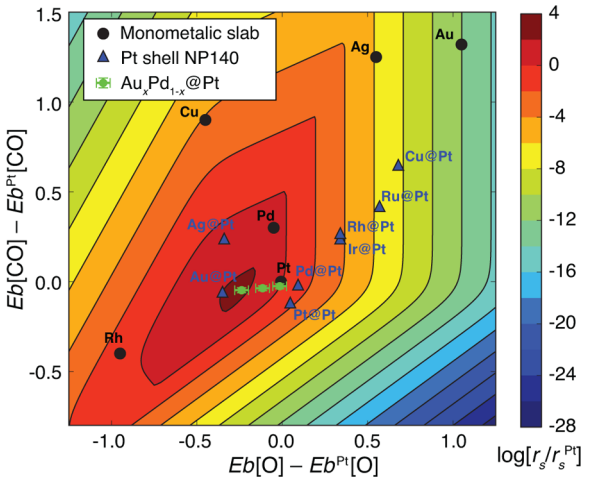

Figure 4. Contour plot of the relative Sabatier rate r_s/r_s^{Pt} on a logarithmic scale as a function of Eb[O] − Eb^{Pt}[O] and Eb[CO] − Eb^{Pt}[CO]. The contours are reproduced from the model in Falsig's work.[15] Of the pure metal slabs (black circles) Pt emerges as the best catalyst. Several single-core@Pt-shell particles also have high activity (blue triangles), with Pd_xAu_{1-x}@Pt NP140 (green points) passing close to the volcano peak.

CO oxidation $\log[r_s/r_s^{Pt}]$ as a function of Eb[O] − Eb^{Pt}[O] and Eb[CO] − Eb^{Pt}[CO] under high-temperature conditions (T = 600 K, p_{O_2} = 0.33 bar, and p_{CO} = 0.67 bar). We chose the Pt(111) slab as our reference because Pt(111) is one of the best catalysts under high-temperature conditions. The two single-core@Pt-shell NP140, Au@Pt and Ag@Pt, emerge as good candidates with activity comparable to or higher that that of Pt(111). It is also possible to tune the activity even higher because there is a gap between these particles and the peak of the volcano.

A quick way to understand how the alloy-core particles can be tuned is to draw a line connecting any two different single-core@Pt-shell NP140 species on the contour plot. If the line intersects a region of high activity, a promising catalytic material can be achieved by alloying the elements of the end point particles in the core. As illustrated in Figure 4, a line between the Au@Pt and Pd@Pt particles passes near the volcano peak. The green scatter points between Au@Pt and Pd@Pt represents Pd_xAu_{1-x}@Pt NP140, with x = 0.25, 0.50, and 0.75. The distribution of Eb[O] and Eb[CO] due to the different alloy cores and binding sites sampled is indicated by the error bars. Several other core element combinations also have the potential to reach the highly active region; a selection is presented in Figure 5. In each cell of the table, the fraction on top is the optimal ratio x^* of metal X in the alloy core, and the blue number in brackets shows the relative rate at this optimal alloy-core composition, which is also the highest activity this X_xY_{1-x}@Pt-shell NP140 can attain. If x^* = 0%, Y@Pt NP140 has the best performance for X_xY_{1-x}@Pt and alloying X in the core will not improve the reactivity, while x^* = 100% indicates that X@Pt is the most reactive composition.

Highlighting one example, the CO oxidation activity of Ag- and Au-core@Pt-shell particles can be enhanced by alloying other transition metals into the core. As shown in Figure 5, the CO oxidation rates of alloy-core@Pt NP140 with core compositions $Au_{0.90}Cu_{0.10}$, $Au_{0.73}Ir_{0.27}$, $Au_{0.65}Pd_{0.35}$, $Au_{0.72}Rh_{0.28}$, $Au_{0.78}Ru_{0.22}$, $Au_{0.73}Pt_{0.27}$, and $Ag_{0.59}Pt_{0.41}$ are 2 orders of magnitude faster than the rate of CO oxidation on the

DOI: 10.1021/cs501176b
ACS Catal. 2015, 5, 655−660

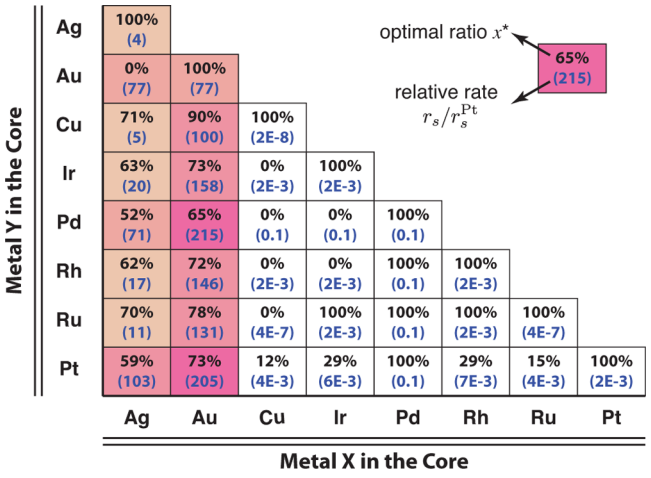

Figure 5. Optimal ratio x^* of metal X alloyed with metal Y in the core of Pt-shelled NP140 for COox estimated from Falsig's Sabatier rate model. The blue numbers in parentheses at the bottom of each cell are the calculated relative Sabatier rates r_s/r_s^{Pt} at the optimal alloy-core composition. The COox rates for $Au_{0.65}Pd_{0.35}$@Pt and $Au_{0.73}Pt_{0.27}$@Pt particles are 200 times that of a Pt(111) slab.

Pt(111) surface. A 200-fold increase over Pt(111) is predicted for $Au_{0.65}Pd_{0.35}$@Pt and $Au_{0.73}Pt_{0.27}$@Pt. In the case of the PdAu@Pt system, Pd@Pt is limited by the O_2 dissociation process (R3) due to its relatively weak O binding. Alloying Au to the Pd core enhances both O and CO binding. On one hand, strengthened O binding facilitates the O_2 dissociation step; on the other hand, the barrier of the CO oxidation step (R4) grows with stronger O and CO binding. The tradeoff between these two effects gives rise to a peak activity at a composition with 65% Au in the core. With less than 65% Au in the core, the overall reactivity is limited by O_2 dissociation; with more than 65% Au, the overall reactivity is limited by CO oxidation by atomic O (R4).

3.5. Stability of Pt and Pd Shell Nanoparticles. Another important consideration for nanoalloy catalysts is their stability. The relative surface energies and adsorbate binding are the two major factors contributing to their thermodynamic stability.[38,39] Previous studies have used the surface segregation energy as a measure of the thermodynamic stability of near-surface alloys.[40,41] Here we follow the same strategy to investigate the stability in terms of the core/shell segregation energy of (111) facet atoms in our Pt- and Pd-shelled nanoparticles with monometallic cores. The core/shell segregation energy is calculated as the energy required to swap one shell atom (Pt or Pd) and its neighboring subsurface atom. The stability under the reaction conditions was also evaluated by considering adsorbates (O, C, H, N, S, CO, and NO) bound at the surface site for which the segregation energy is calculated.

Figure 6 shows the calculated segregation energy of Pt shell nanoparticles with and without adsorbates. Results of Pd shell nanoparticles are similar and can be found in Figure S5 in the Supporting Information. The majority of the systems considered on the plot are thermodynamically stable, with positive segregation energies. Without adsorbates, all of the Pt nanoparticles are thermodynamically stable with positive segregation energy except for Cu@Pt. Ag and Au are less reactive than Pt, so that the presence of adsorbed species increases the energetic cost of core/shell swapping, resulting in enhanced stability. Ir, Rh, and Ru bind the adsorbates more strongly than Pt, and their presence lowers the energy required

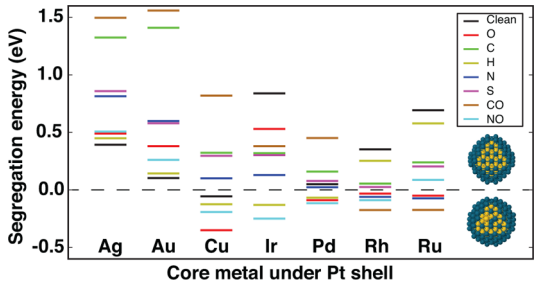

Figure 6. Calculated segregation energy of Pt shell nanoparticles with and without adsorbates (O, C, H, N, S, CO, and NO). The insets indicate the preferred structures according to the sign of the segregation energy (adsorbates are not shown).

for segregation. Due to the similarity of Pd and Pt, all segregation energies of Pd@Pt are close to 0, except in the case of CO, where extra stability is gained. For HER, Ag, Au, Rh, and Ru in the core of Pt shell nanoparticles are stable both under vacuum and in a H-rich environment.

For the systems identified as good candidates for CO oxidation, AgPd@Pt and AuPd@Pt, Ag and Au are stable under the Pt shell under all conditions. Pd@Pt has a positive segregation energy under vacuum and in a CO-rich environment. Although the thermodynamic stability of the Pd@Pt nanoparticle is reduced with surface-bound oxygen species, it has been reported that introducing Au or Ag to the Pd core can enhance the stability and durability of a Pt surface layer under ORR conditions.[11,42] It is also worth noting that nanoparticles with negative segregation energy may still be kinetically stable. For example, Cu@Pt adsorbed by O has the most negative segregation energy in the systems we investigated. However, Cu was found to be kinetically stable in the core of PdCu@Pt particles and more active in ORR experiments than Pd@Pt particles.[43]

4. CONCLUSIONS

We have shown general linear correlations between the adsorbate binding energy to the shell of an alloy-core@shell nanoparticle and the composition of the core. This relationship allows for interpolation of the properties of single-core@shell particles and an approach for tuning the catalytic activity of the particle. Application to the HER and COox reactions reveals a series of promising catalysts. A previously reported $Pt_{0.5}Ru_{0.5}$@Pd for HER has been identified by this approach; many other predictions have not yet been tested. While our demonstration is only for the HER and COox reactions, this method of tuning catalytic activity provides a general framework for computational optimization of alloy-core@shell nanoparticles for other reactions of interest.

■ ASSOCIATED CONTENT

Supporting Information

The following file is available free of charge on the ACS Publications website at DOI: 10.1021/cs501176b.

Details about the reference energy for the adsorbates, the number of samples in each random alloy core composition, the linear binding trends of individual adsorbate, a comparison of factors influencing the PdAu@Pt and PdIr@Pt *d*-band of the Pt shell, and a stability analysis of Pd-shelled NP140 (PDF)

DOI: 10.1021/cs501176b
ACS Catal. 2015, 5, 655−660

AUTHOR INFORMATION

Corresponding Author

*E-mail for G.H.: henkelman@utexas.edu.

Notes

The authors declare no competing financial interest.

ACKNOWLEDGMENTS

This work was supported by the U.S. Department of Energy, Office of Basic Energy Sciences (Contract No. DE-FG02-13ER16428). Computing time was provided by the National Energy Research Scientific Computing Center and the Texas Advanced Computing Center at the University of Texas at Austin.

REFERENCES

(1) Zhang, L.; Iyyamperumal, R.; Yancey, D. F.; Crooks, R. M.; Henkelman, G. *ACS Nano* **2013**, *7*, 9168−9172.
(2) Zhang, L.; Henkelman, G. *J. Phys. Chem. C* **2012**, *116*, 20860−20865.
(3) Tang, W.; Henkelman, G. *J. Chem. Phys.* **2009**, *130*, 194504.
(4) Tang, W.; Zhang, L.; Henkelman, G. *J. Phys. Chem. Lett.* **2011**, *2*, 1328−1331.
(5) Wang, C.; Chi, M.; Li, D.; Strmcnik, D.; van der Vliet, D.; Wang, G.; Komanicky, V.; Chang, K.-C.; Paulikas, A. P.; Tripkovic, D.; Pearson, J.; More, K. L.; Markovic, N. M.; Stamenkovic, V. R. *J. Am. Chem. Soc.* **2011**, *133*, 14396−14403.
(6) Stamenkovic, V. R.; Mun, B. S.; Arenz, M.; Mayrhofers, K. J. J.; Lucas, C. A.; Wang, G.; Ross, P. N.; Marković, N. M. *Nat. Mater.* **2007**, *6*, 241−247.
(7) Stamenkovic, V. R.; Mun, B. S.; Mayrhofer, K. J. J.; Ross, P. N.; Markovic, N. M. *J. Am. Chem. Soc.* **2006**, *128*, 8813−8819.
(8) Stamenkovic, V.; Mun, B. S.; Mayrhofer, K. J.; Ross, P. N.; Markovic, N. M.; Rossmeisl, J.; Greeley, J.; Nørskov, J. K. *Angew. Chem., Int. Ed.* **2006**, *45*, 2897−2901.
(9) Yancey, D. F.; Carino, E. V.; Crooks, R. M. *J. Am. Chem. Soc.* **2010**, *132*, 10988−10989.
(10) Yancey, D. F.; Zhang, L.; Crooks, R. M.; Henkelman, G. *Chem. Sci.* **2012**, *3*, 1033−1040.
(11) Sasaki, K.; Wang, J.; Naohara, H.; Marinkovic, N.; More, K.; Inada, H.; Adzic, R. *Electrochim. Acta* **2010**, *55*, 2645−2652.
(12) Carino, E. V.; Crooks, R. M. *Langmuir* **2011**, *27*, 4227−4235.
(13) Sasaki, K.; Naohara, H.; Choi, Y.; Cai, Y.; Chen, W.-F.; Liu, P.; Adzic, R. R. *Nat. Commun.* **2012**, *3*, 1115.
(14) Koenigsmann, C.; Sutter, E.; Adzic, R. R.; Wong, S. S. *J. Phys. Chem. C* **2012**, *116*, 15297−15306.
(15) Falsig, H.; Hvolbæk, B.; Kristensen, I. S.; Jiang, T.; Bligaard, T.; Christensen, C. H.; Nørskov, J. K. *Angew. Chem., Int. Ed.* **2008**, *47*, 4835−4839.
(16) Xu, Y.; Lausche, A. C.; Wang, S.; Khan, T. S.; Abild-Pedersen, F.; Studt, F.; Nørskov, J. K.; Bligaard, T. *New J. Phys.* **2013**, *15*, 125021.
(17) Lausche, A. C.; Medford, A. J.; Khan, T. S.; Xu, Y.; Bligaard, T.; Abild-Pedersen, F.; Nørskov, J. K.; Studt, F. *J. Catal.* **2013**, *307*, 275−282.
(18) Yoo, J. S.; Abild-Pedersen, F.; Nørskov, J. K.; Studt, F. *ACS Catal.* **2014**, *4*, 1226−1233.
(19) Kresse, G. *Phys. Rev. B* **2000**, *62*, 8295−8305.
(20) Kresse, G.; Hafner, J. *Surf. Sci.* **2000**, *459*, 287−302.
(21) Blöchl, P. E. *Phys. Rev. B* **1994**, *50*, 17953.
(22) Kresse, G.; Joubert, D. *Phys. Rev. B* **1999**, *59*, 1758.
(23) Hammer, B.; Hansen, L. B.; Nørskov, J. K. *Phys. Rev. B* **1999**, *59*, 7413−7421.
(24) Li, L.; Larsen, A. H.; Romero, N. A.; Morozov, V. A.; Glinsvad, C.; Abild-Pedersen, F.; Greeley, J.; Jacobsen, K. W.; Nørskov, J. K. *J. Phys. Chem. Lett.* **2013**, *4*, 222−226.
(25) Peterson, A. A.; Grabow, L. C.; Brennan, T. P.; Shong, B.; Ooi, C.; Wu, D. M.; Li, C. W.; Kushwaha, A.; Medford, A. J.; Mbuga, F.; Li, L.; Nørskov, J. K. *Top. Catal.* **2012**, *55*, 1276−1282.
(26) Mason, S. E.; Grinberg, I.; Rappe, A. M. *Phys. Rev. B* **2004**, *69*, 161401.
(27) Abild-Pedersen, F.; Greeley, J.; Studt, F.; Rossmeisl, J.; Munter, T. R.; Moses, P. G.; Skúlason, E.; Bligaard, T.; Nørskov, J. K. *Phys. Rev. Lett.* **2007**, *99*, 016105.
(28) Fernández, E. M.; Moses, P. G.; Toftelund, A.; Hansen, H. A.; Martnez, J. I.; Abild-Pedersen, F.; Kleis, J.; Hinnemann, B.; Rossmeisl, J.; Bligaard, T.; Nørskov, J. K. *Angew. Chem., Int. Ed.* **2008**, *47*, 4683−4686.
(29) Bligaard, T.; Nørskov, J.; Dahl, S.; Matthiesen, J.; Christensen, C.; Sehested, J. *J. Catal.* **2004**, *224*, 206−217.
(30) Nørskov, J. K.; Bligaard, T.; Rossmeisl, J.; Christensen, C. H. *Nat. Chem.* **2009**, *1*, 37−46.
(31) Nørskov, J. K.; Abild-Pedersen, F.; Studt, F.; Bligaard, T. *Proc. Natl. Acad. Sci. U.S.A.* **2011**, *108*, 937−943.
(32) Nørskov, J. K.; Rossmeisl, J.; Logadottir, A.; Lindqvist, L.; Kitchin, J. R.; Bligaard, T.; Jónsson, H. *J. Phys. Chem. B* **2004**, *108*, 17886−17892.
(33) Nørskov, J. K.; Bligaard, T.; Logadottir, A.; Kitchin, J. R.; Chen, J. G.; Pandelov, S.; Stimming, U. *J. Electrochem. Soc.* **2005**, *152*, J23−J26.
(34) Parsons, R. *Trans. Faraday Soc.* **1958**, *54*, 1053−1063.
(35) Greeley, J.; Nørskov, J. K.; Kibler, L. A.; El-Aziz, A. M.; Kolb, D. M. *ChemPhysChem* **2006**, *7*, 1032−1035.
(36) Greeley, J.; Jaramillo, T. F.; Bonde, J.; Chorkendorff, I.; Norskov, J. K. *Nat. Mater.* **2006**, *5*, 909−913.
(37) Liu, Z.-P.; Hu, P.; Alavi, A. *J. Am. Chem. Soc.* **2002**, *124*, 14770−14779.
(38) Wang, L.-L.; Johnson, D. D. *J. Am. Chem. Soc.* **2009**, *131*, 14023−14029.
(39) Ferrando, R.; Jellinek, J.; Johnston, R. L. *Chem. Rev.* **2008**, *108*, 845−910.
(40) Ruban, A. V.; Skriver, H. L.; Nørskov, J. K. *Phys. Rev. B* **1999**, *59*, 15990−16000.
(41) Greeley, J.; Mavrikakis, M. *Catal. Today* **2006**, *111*, 52−58.
(42) Yang, J.; Yang, J.; Ying, J. Y. *ACS Nano* **2012**, *6*, 9373−9382.
(43) Cochell, T.; Manthiram, A. *Langmuir* **2012**, *28*, 1579−1587.

DOI: 10.1021/cs501176b
ACS Catal. 2015, 5, 655−660